Supporting Information

Ni–NC and Fe–NC Single-Atom Catalysts on Ti-doped Hematite for Selective Photoelectrochemical Glycerol Oxidation

Mengya Yang[a], Hanzhi Ye[a], Zhe Meng[b], Angus Pedersen[a], Joseph Parker[c], Sarah J. Haigh[c], Hui Luo[d], Henrik H. Kristoffersen[b], Jan Rossmeisl[b], Magda Magdalena Titirici[a,e], Anna Hankin[a], Jesús Barrio[a], Salvador Eslava [a*]*

[a] Department of Chemical Engineering and Centre for Processable Electronics, Imperial College London, SW7 2AZ, London, United Kingdom

[b] Department of Chemistry, University of Copenhagen, Copenhagen 2100, Denmark

[c] Department of Materials and National Graphene Institute, University of Manchester, M13 9PL, United Kingdom

[d] School of Engineering, University of Surrey, Guildford, GU2 7XH, United Kingdom

[e] Advanced Institute for Materials Research (WPI-AIMR), Tohoku University, 2-1-1 Katahira,
Aoba-ku, Sendai, Miyagi, 980-8577, Japan

*E-mail: j.barrio-hermida@imperial.ac.uk; s.eslava@imperial.ac.uk

Keywords: Single-atom catalysts; hematite photoanodes; photoelectrochemical glycerol oxidation; product selectivity; density functional theory; renewable energy conversion

Experimental Section

Preparation of M–NC (M = Ni or Fe) single-atom catalysts

The M–NC materials were synthesized following our previously reported method.[1, 2] Briefly, 2,4,6-triaminopyrimidine (TAP, 97%, Sigma-Aldrich) and $MgCl_2 \cdot 6H_2O$ (99%, Sigma-Aldrich) were mixed at a weight ratio of 1:8, respectively, and pyrolyzed at 900 °C for 1 h under a N_2 atmosphere (flow rate: 300 mL min^{-1}; heating rate: 5 °C min^{-1}), followed by natural cooling to room temperature. The resulting solid was ground with a pestle and mortar and then washed overnight in 2 M HCl, thoroughly rinsed with deionized water, and dried at 80 °C. To introduce metal single atoms, 60 mg of the TAP-derived support was dispersed in 75 mL methanol and mixed with 75 mL of a 25 mM metal chloride solution ($FeCl_2$, 98%, Sigma-Aldrich, or $NiCl_2 \cdot 4H_2O$, 99.9%, Sigma-Aldrich). The mixture was refluxed at 85 °C for 24 h, followed by washing with 0.5 M H_2SO_4 to remove aggregated metal species. The solid was then filtered, rinsed thoroughly with distilled water, and dried at 80 °C. The resulting catalysts were denoted as M–NC (where M = Fe or Ni).

Preparation of Ti–Fe_2O_3 films

Ti–Fe_2O_3 films were synthesized on fluorine-doped tin oxide (FTO)-coated glass substrates via a hydrothermal method followed by annealing in air, as reported previously.[3] Prior to synthesis, the FTO substrates were cleaned by ultrasonication sequentially in detergent, isopropanol (IPA), and deionized water for 10 min each. A 20 mL aqueous precursor solution was prepared by dissolving 0.6 g $FeCl_3$ (97%, Sigma-Aldrich) and 1.7 g $NaNO_3$ (99%, Sigma-Aldrich), with the pH adjusted to 3 using 1 M HCl. Subsequently, 5 mL of an ethanol solution containing 35 mg $TiCl_4$ was added. The resulting solution was transferred to a 50 mL Teflon-lined stainless-steel autoclave. The cleaned FTO substrates (2.5 × 4 cm^2) were immersed in the solution with the conductive side facing downward at an angle of approximately 30°. The autoclaves were sealed and heated at 95 °C for 7.5 h to promote the growth of Ti-doped β-FeOOH films. After cooling to room temperature, the films were annealed in air with a heating rate of 5 °C min^{-1} to 550 °C and held for 2 h, followed by further heating to 800 °C (5 °C min^{-1}) and holding for 20 min. The samples were then allowed to cool naturally to room temperature inside the furnace, yielding Ti–Fe_2O_3 films.

Preparation of Ti–Fe_2O_3/Ni–NC and Ti–Fe_2O_3/Fe–NC photoanodes

Ti–Fe_2O_3/Ni–NC and Ti–Fe_2O_3/Fe–NC photoanodes were prepared by spin coating. A catalyst ink was prepared by dispersing 4 mg of Ni–NC or Fe–NC in a mixed solvent of deionized water (500 μL) and ethanol (500 μL), followed by bath sonication for 30 min to obtain a homogeneous suspension. Spin coating was performed at 3000 rpm for 30 s, with a controlled drop-casting volume of 50 μL per coating cycle. The coating process was repeated between one and four times to control catalyst loading. After coating, the samples were heated on a hot plate at 110 °C for 1 h to dry the films and improve contact formation. Optimal photoelectrochemical performance was achieved with two spin-coating cycles, corresponding to a total ink volume of 100 μL.

Characterizations

All (photo)electrochemical measurements were performed using a potentiostat (IviumStat, Ivium Technologies) in an electrolyte containing 0.5 M glycerol and 1 M NaOH (pH = 13.7) under simulated sunlight (Xe lamp equipped with an AM 1.5G filter, 100 mW cm^{-2}, 1 sun). A three-electrode photoelectrochemical (PEC) cell with a quartz window was employed. The prepared photoanodes served as the working electrode, with a Pt filament and an Ag/AgCl electrode (3 M KCl) used as the counter and reference electrodes, respectively. (Photo)current–potential (j–V) curves were recorded by scanning the applied potential from +0.4 to +1.7 V_{RHE} at a scan rate of 10 mV s^{-1}. All potentials measured versus Ag/AgCl ($V_{Ag/AgCl}$) were converted to the reversible hydrogen electrode (V_{RHE}) scale using the Nernst equation:

$$E_{\mathrm{RHE}} = E_{\mathrm{Ag/AgCl}} + 0.059 \times \mathrm{pH} + E^{\circ}_{\mathrm{Ag/AgCl}} \qquad (1)$$

where $E^{\circ}_{\mathrm{Ag/AgCl}} = 0.1976$ V.

The incident photon-to-current efficiency (IPCE) was measured in 0.5 M glycerol and 1 M KOH at an applied potential of +1.23 V_{RHE} using a Xe lamp coupled with a monochromator (LOT Quantum Design). IPCE values were calculated according to:

$$\mathrm{IPCE}(\%) = \frac{1240 \times j_{\mathrm{ph}}}{\lambda \times P_{\lambda}} \qquad (2)$$

where λ(nm) is the incident monochromatic wavelength, j_{ph}(mA cm^{-2}) is the photocurrent density measured under monochromatic illumination, and P_{λ}(mW cm^{-2}) is the incident light power density at wavelength λ.

The crystalline structure and phase composition of the samples were characterized by X-ray diffraction (XRD, X'Pert Pro PANalytical diffractometer, Cu K_{α} radiation, 40 kV, 20 mA, 2θ range: 10–80°). Surface chemical composition and electronic states were analyzed using X-ray photoelectron spectroscopy (XPS, Thermo Fisher K-Alpha^{+} spectrometer with monochromated Al Kα radiation). All

XPS spectra were calibrated using the C *1s* peak. Sample morphologies were examined by field-emission scanning electron microscopy (FE-SEM, LEO Gemini 1525).

Time-of-flight secondary ion mass spectrometry (ToF-SIMS) measurements were carried out using an ION-TOF V instrument. Fresh and post-reaction Ti–Fe_2O_3/Ni–NC photoanodes were analyzed directly on their FTO substrates, which were mounted on double-sided tape, while NC powder samples were pressed onto double-sided tape. Post-reaction samples were obtained after PEC GOR testing for 2 h at +1.23 V_{RHE} under 1 sun illumination. Prior to analysis, samples were sputtered over a 500 × 500 μm^2 area using a non-interlaced 10 keV Ar_n^+ ($n \approx 1600–1700$) cluster ion beam at ~11 nA for one sputter frame (pause time: 1 s), corresponding to a dose density of ~10^{15} ions cm^{-2}.

ToF-SIMS spectra were acquired using a Bi_3^+ primary ion beam (25 keV, 0.5 pA, 5 µm spot size) for 25 min, with a cycle time of 100 µs and a raster area of 100 µm × 100 µm (256 × 256 pixels, sawtooth mode). Negative ion spectra were calibrated using C_1^-–C_{10}^- and $Fe_2O_3^-$ reference peaks, with a mass deviation below 100 ppm. Data analysis was performed using SurfaceLab 7 software. Peak intensities were normalized to the total ion count over the full mass spectrum (0–870 amu). Measurements were conducted at two distinct locations on each sample where Ni–NC was present. Algebraic deconvolution of the ^{58}Ni and ^{60}Ni isotopes was carried out following the method reported by Sarma *et al.*[2]

Faradaic efficiency calculations

Faradaic efficiencies (FEs) for glyceric acid (GLA), glycolic acid (GA), and formic acid (FA) were calculated from the amounts of products formed during 2 h of photoelectrochemical glycerol oxidation. Product concentrations were quantified by HPLC and converted to moles according to:

$$N_\mathrm{i} = C_\mathrm{i} \times V$$

where N_i is the number of moles of product i, C_i is the HPLC-determined concentration (mol L^{-1}), and V is the electrolyte volume (L).

The Faradaic efficiency (FE) for each product was calculated using:

$$FE_\mathrm{i}\,(\%) = (n_\mathrm{i} \times F \times N_\mathrm{i} \,/\, Q_\mathrm{tot}) \times 100$$

where n_i is the number of electrons transferred for the formation of product i, F is the Faraday constant (96485 C mol^{-1}), N_i is the number of moles of product formed, and Q_tot is the total charge passed during electrolysis.

The total charge passed was determined by integrating the current over the 2h reaction period at respective applied potentials:

$$Q_{\mathrm{tot}} = \int_{0}^{2h} I(t)\, dt$$

where $I(t)$ is the measured current as a function of time.

The electron-transfer numbers were assigned based on the oxidation-state change from glycerol to the corresponding products, giving n = 4 for glyceric acid (GLA), n = 10/3 for glycolic acid (GA), and n = 8/3 for formic acid (FA).[4] The FE values therefore represent the fraction of the total charge contributing to the formation of each oxidation product. The sum of the FEs for individual products was used to evaluate the selectivity of the glycerol oxidation reaction and the contribution of competing side reactions, such as oxygen evolution.

Computational Section

Density functional theory (DFT) calculations were performed to evaluate the energetics of glycerol electro-oxidation intermediates and products. In the computational models, glycerol-derived intermediates were adsorbed on a single metal atom (Ni or Fe) coordinated to a metal–N_4–pyridine-doped graphene surface, representing the Ni–NC or Fe–NC catalyst. Periodic slab models were constructed with a vacuum spacing of 24 Å to eliminate interlayer interactions. Atomic structures were generated using the Atomic Simulation Environment (ASE).[5] All DFT calculations were carried out using the GPAW package[6, 7] with the revised Perdew–Burke–Ernzerhof (RPBE) exchange–correlation functional.[8] A plane-wave basis set with cutoff energy of 400 eV and a 3 × 3 × 1 Monkhorst–Pack k-point mesh were employed. Spin-polarized calculations were performed by initializing the Fe and Ni atoms with magnetic moments appropriate for their typical electronic configurations. These moments were allowed to evolve during structural relaxation, adapting to the structure and adsorbed intermediates. The atomic structures are relaxed to a maximum force of 0.10 eV $Å^{-1}$ on each atom.

To elucidate glycerol electro-oxidation pathways on Ni–NC and Fe–NC surfaces, two elementary reaction types were considered. The first involves dehydrogenation (Equation 3), in which a hydrogen atom is removed from the adsorbate ($C_3H_yO_x$), yielding a more oxidized intermediate ($C_3H_{y-1}O_x$) and producing ½ H_2 in the gas phase:

$$\mathrm{C_3H_yO_x \rightarrow C_3H_{y-1}O_x + H^+(aq) + e^-} \qquad (3)$$

The second reaction type corresponds to hydroxyl (OH) incorporation (Equation 4), which produces a more oxidized intermediate ($C_3H_{y+1}O_{x+1}$) through the consumption of one liquid H_2O molecule and formation of ½ H_2:

$$\mathrm{C_3H_yO_x + H_2O(l) \rightarrow C_3H_{y+1}O_{x+1} + \frac{1}{2}H_2(g)} \qquad (4)$$

While most computational studies of glycerol oxidation focus on dehydrogenation reactions (Equation 3), [9-13] hydroxyl incorporation steps (Equation 4) have also been reported and were therefore included here.[14-16]

In electrochemical environments, proton–electron [H^+(aq) and e^-] pairs are produced instead of molecular hydrogen gas. This effect was incorporated using the computational hydrogen electrode (CHE) model,[17, 18] which relates the free energy of a proton–electron pair to the electrochemical potential on the reversible hydrogen electrode (RHE) scale:

$$\Delta G(\mathrm{H^+(aq) + e^-}) = \frac{1}{2}\Delta G(\mathrm{H_2}) - eU_{\mathrm{vsRHE}} \qquad (5)$$

Unless otherwise stated, all reaction free energies were evaluated at $U_{\mathrm{vs\,RHE}} = 0\,\mathrm{V}$. At applied potentials $U_{\mathrm{vs\,RHE}} > 0$, both reaction types (Equations 3 and 4) are stabilized by a term of $-eU_{\mathrm{vs\,RHE}}$.

The DFT reaction energies of adsorbed intermediates were calculated according to:

$$\Delta E_{\mathrm{intermediate}} = E_{\mathrm{surface+intermediate}} - E_{\mathrm{surface}} - E_{\mathrm{glycerol}} + n_{\mathrm{H_2}}E_{\mathrm{H_2}} - m_{\mathrm{H_2O}}E_{\mathrm{H_2O}} \qquad (6)$$

where $E_{\mathrm{surface+intermediate}}$ and E_{surface} are the DFT energies of the catalyst surface with and without the adsorbed intermediate, respectively. E_{glycerol}, $E_{\mathrm{H_2}}$, and $E_{\mathrm{H_2O}}$ correspond to the gas-phase energies of glycerol, H_2, and H_2O. $n_{\mathrm{H_2}}$ and $m_{\mathrm{H_2O}}$ represent the number of H_2 molecules produced and H_2O molecules consumed, respectively, when converting glycerol to the intermediate in question.

Entropy differences, zero-point energy differences, or heating enthalpy differences were not calculated. Instead, literature-derived free energy corrections established for CH_3O^* reduction to $COOH^*$ were adopted.[19] These corrections comprise three type equation 3 reaction steps with an average free energy correction of $\Delta G_{\mathrm{eq3}}^{corr} = -0.32\mathrm{eV}$ (standard deviation of 0.05 eV), and one type equation 4 reaction step with a free energy correction of $\Delta G_{\mathrm{eq4}}^{corr} = +0.38$ eV. We adopt the same free energy corrections, even though we study glycerol oxidation instead of methanol oxidation, and approximated the free energy differences of the adsorbed intermediates $\Delta G_{intermediate}$ by Equation 7.

$$\Delta G_{\mathrm{intermediate}} = \Delta E_{\mathrm{intermediate}} + n_{\mathrm{eq3}} \Delta G_{\mathrm{eq3}}^{\mathrm{corr}} + m_{\mathrm{eq4}} \Delta G_{\mathrm{eq4}}^{\mathrm{corr}} \qquad (7)$$

where n_{eq3} and m_{eq4} denote the number of dehydrogenation and OH incorporation steps, respectively, required to form a given intermediate.

The gas-phase H_2O pressure was set to 0.0035 MPa, such that the free energy of gas-phase H_2O equals that of liquid water under ambient conditions.[17] It should be noted that solvation effects and constant-potential electrochemical interfaces were not modeled. Solvation effects can be especially large, but unfortunately, they are also prohibitively computationally expensive to accurately account for. [20]

All DFT calculations and Python scripts used in this work are publicly available at: https://erda.ku.dk/archives/a6928c8acbd736a52956d981c0893d9e/published-archive.html

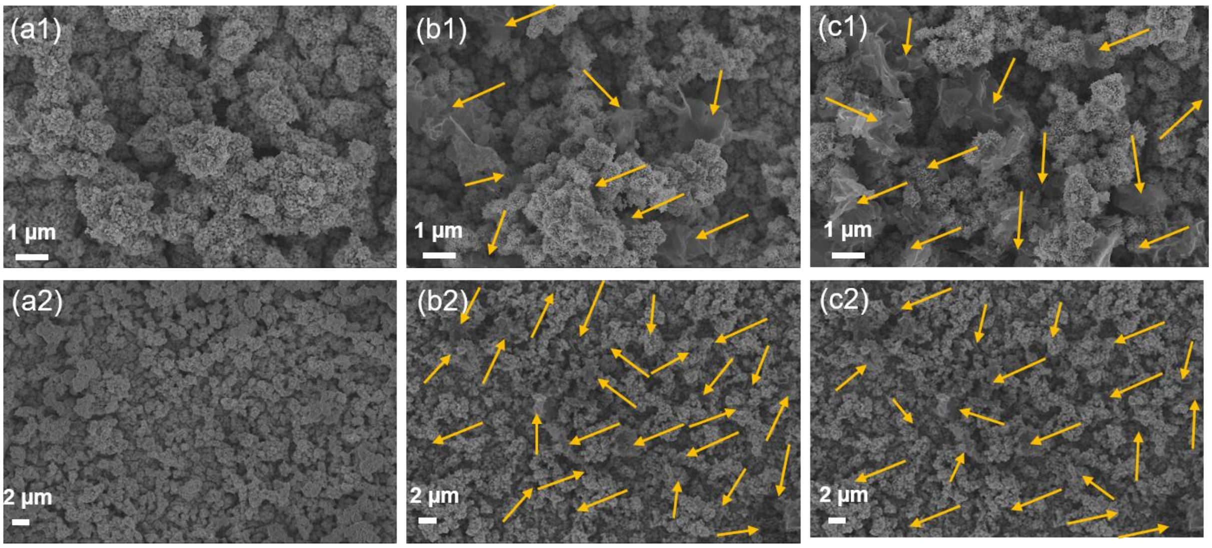

Figure S1. FE-SEM micrographs, acquired using the in-column secondary electron (InLens) detector, of (a1-2) Ti–Fe_2O_3, (b1-2) Ti–Fe_2O_3/Ni–NC, and (c1-2) Ti–Fe_2O_3/Fe–NC with orange arrows on flakes.

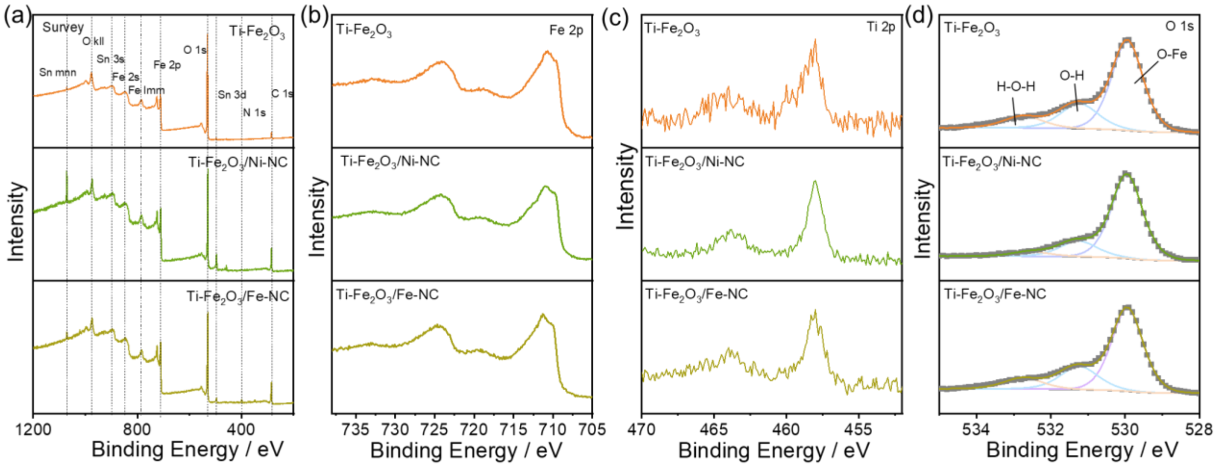

Figure S2. (a) XPS survey spectra and high-resolution XPS spectra of (b) Fe *2p*, (c) Ti *2p*, and (d) O *1s* for Ti–Fe_2O_3, Ti–Fe_2O_3/Ni–NC, and Ti–Fe_2O_3/Fe–NC.

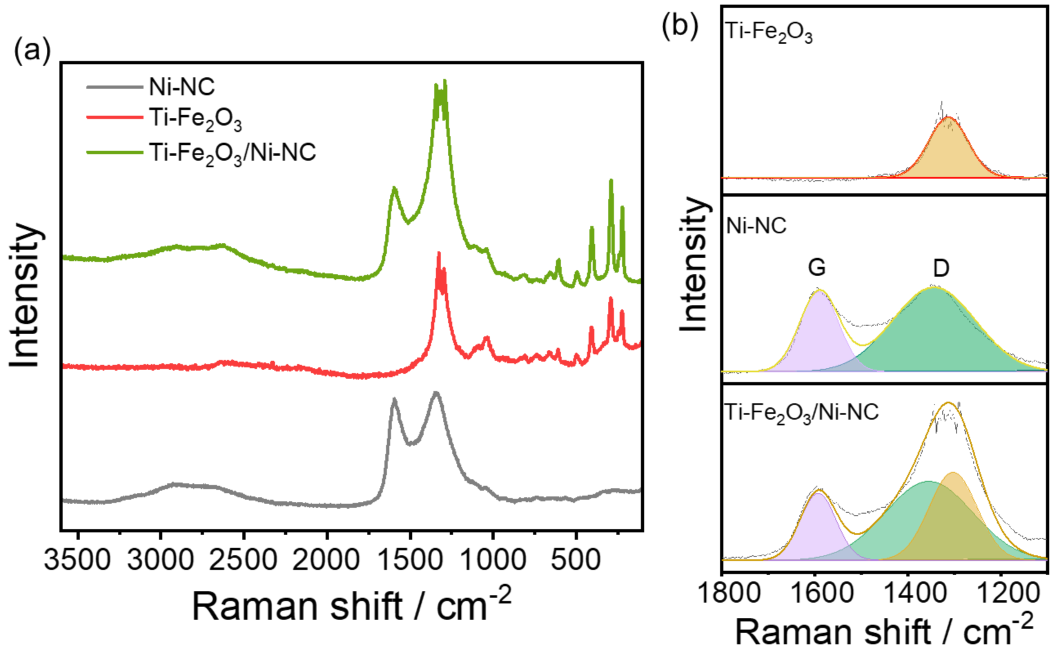

Figure S3. (a) Raman spectra for Ni-NC, Ti-Fe_2O_3 and Ti-Fe_2O_3/Ni-NC. (b)Deconvoluted Raman spectra for for Ni-NC, Ti-Fe_2O_3 and Ti-Fe_2O_3/Ni-NC.

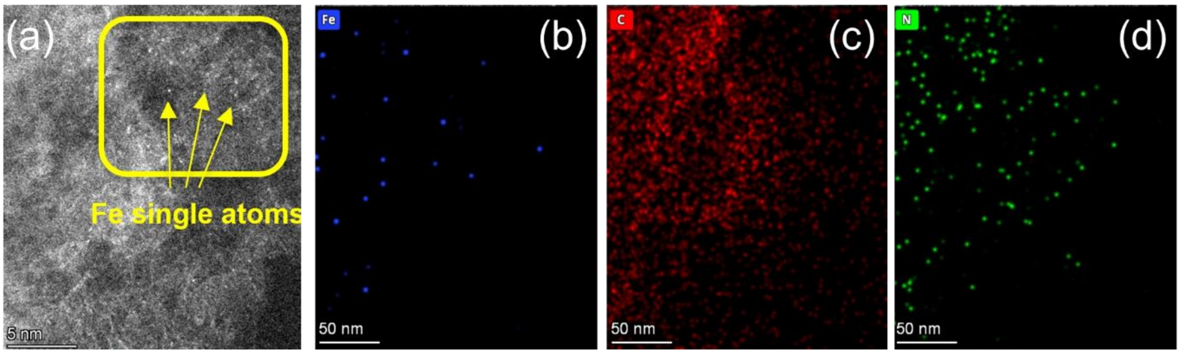

Figure S4. (a) HAADF-STEM image and atomic resolution EDX elemental maps for Fe (b), C (c), and N (d) of Fe-NC. Reproduced from ref [21] with permission from Wiley and the authors.

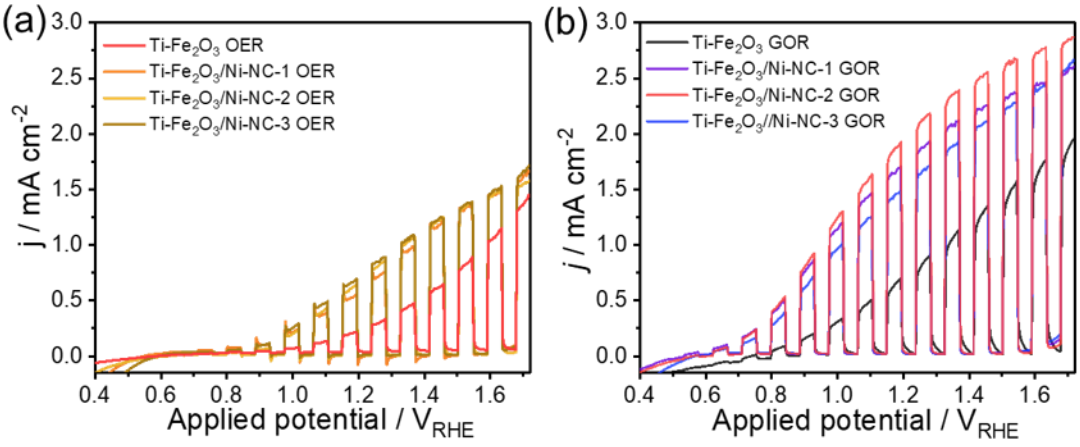

Figure S5. (Photo)current–potential (j–V) curves of Ti–Fe_2O_3 and Ti–Fe_2O_3/Ni–NC-n (n = 1, 2, and 3, corresponding to 1, 2, and 4 spin-coating cycles, respectively) measured in (a) 1 M NaOH and (b) 1 M NaOH with 0.5 M glycerol. All measurements were performed under 1 sun illumination (Xe lamp, AM 1.5G filter, 100 mW cm^{-2}) with chopped light at a scan rate of 10 mV s^{-1}.

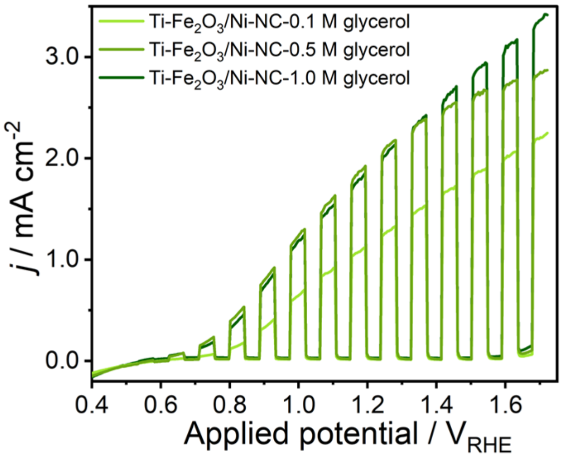

Figure S6. (Photo)current–potential (j–V) curves of Ti–Fe_2O_3/Ni-NC measured in 1M NaOH and different concentrations of glycerol. 0.1 M glycerol appears insufficient, while 1.0 M appears in excess; therefore, 0.5 M glycerol was chosen for further studies.

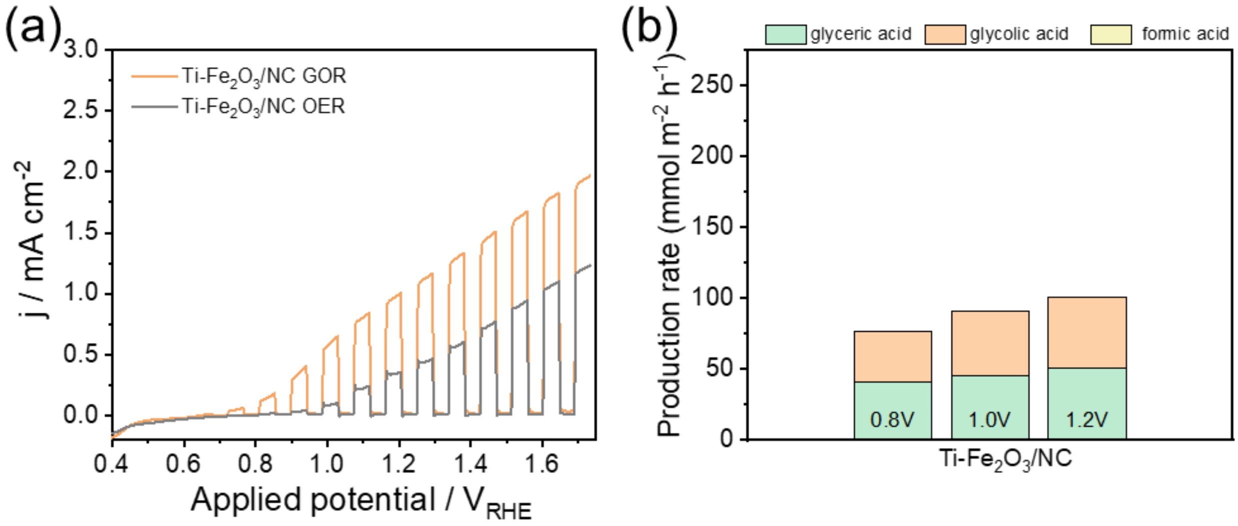

Figure S7. (a) (Photo)current–potential (j–V) curves of Ti–Fe_2O_3/NC measured in 1 M NaOH and in 0.5 M glycerol + 1 M NaOH. (b) Photoelectrocatalytic production rates of glycerol oxidation products on Ti–Fe_2O_3/NC photoanodes at applied potentials of +0.8, +1.0, and +1.2 V_{RHE}.

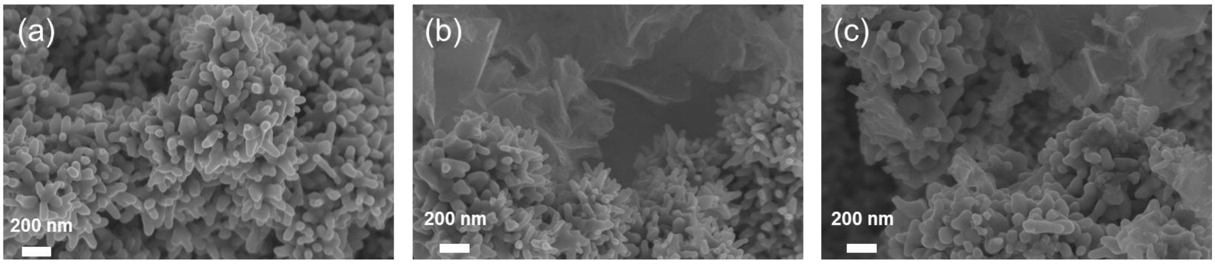

Figure S8. FE-SEM micrographs, acquired using the in-column secondary electron (InLens) detector, of (a) Ti–Fe_2O_3, (b) Ti–Fe_2O_3/Ni–NC, and (c) Ti–Fe_2O_3/Fe–NC after PEC operation for 2 h at +1.23 V_{RHE} in 0.5 M glycerol and 1 M NaOH under 1 sun illumination.

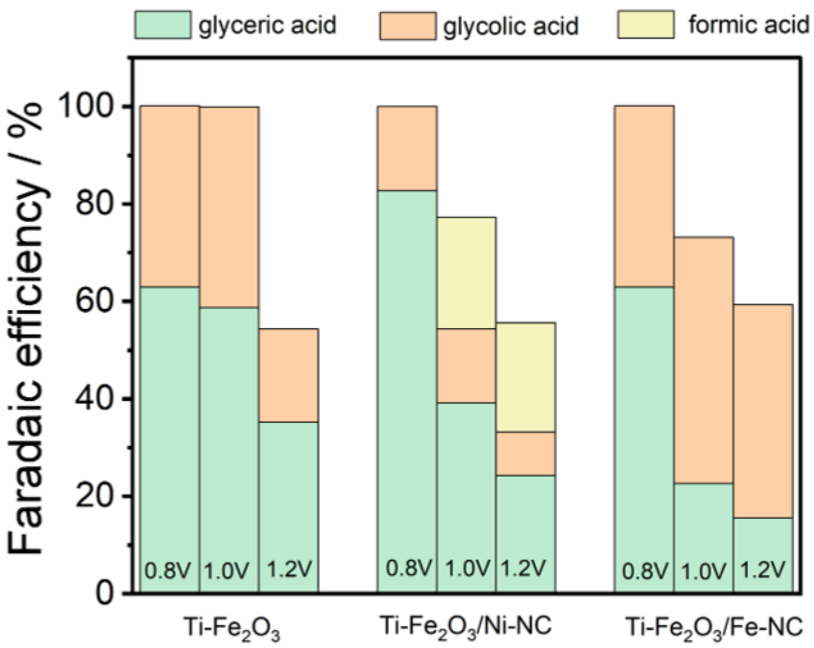

Figure S9. Faradic efficiencies toward glyceric acid (GLA), glycolic acid (GA), and formic acid (FA) afer 2 h GOR reaction at different applied potentials.

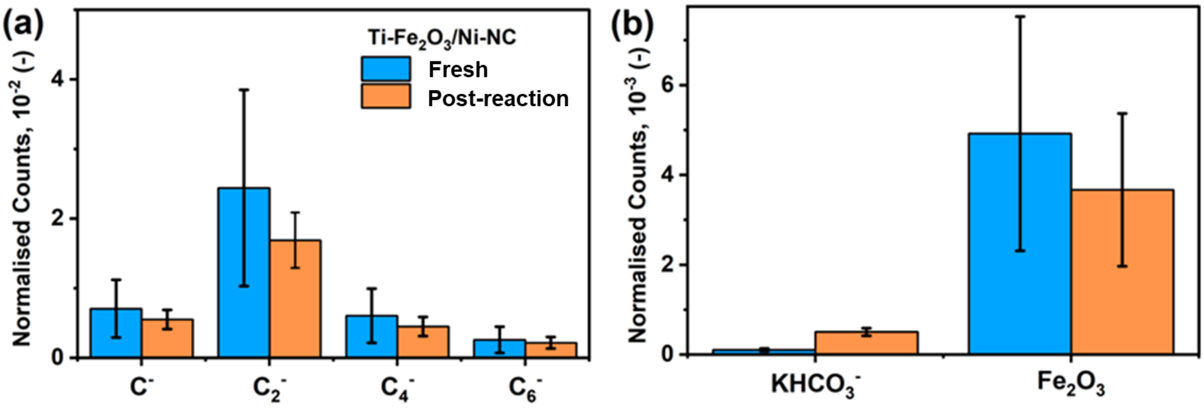

Figure S10. Negative-polarity ToF-SIMS analysis of fresh and post–reaction Ti–Fe$_2$O$_3$/Ni–NC photoanodes. The reaction was PEC GOR for 2 h at +1.23 V$_{RHE}$ under 1 sun illumination. Normalized fragment ion counts (normalized to total ion counts) for (a) calibration peaks and (b) reference peaks. The bars represent the mean values, and the error bars the deviation of two measurements at distinct locations where Ni–NC was visibly deposited.

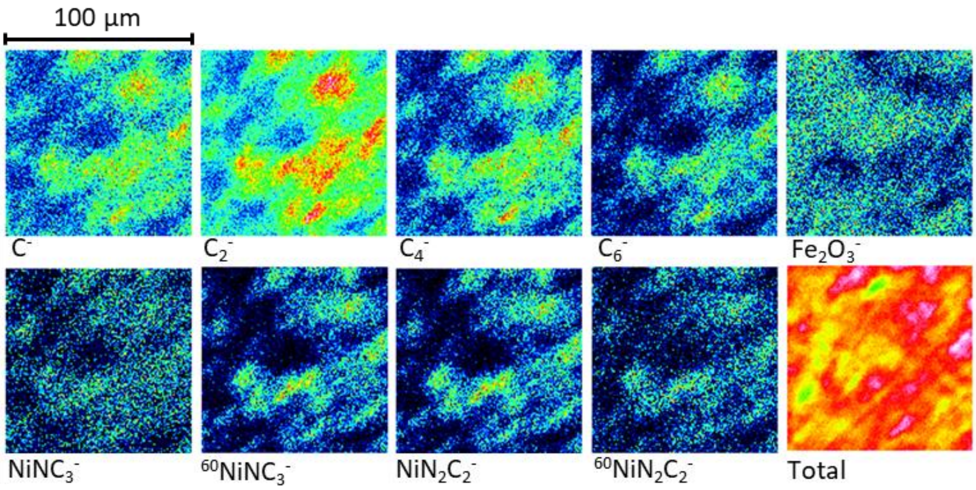

Figure S11. Negative polarity ToF-SIMS fragment mapping counts of Ti-Fe_2O_3/Ni-NC tested after 2 h at +1.23 V_{RHE} in 0.5 M glycerol + 1 M NaOH under 1 sun illumination.

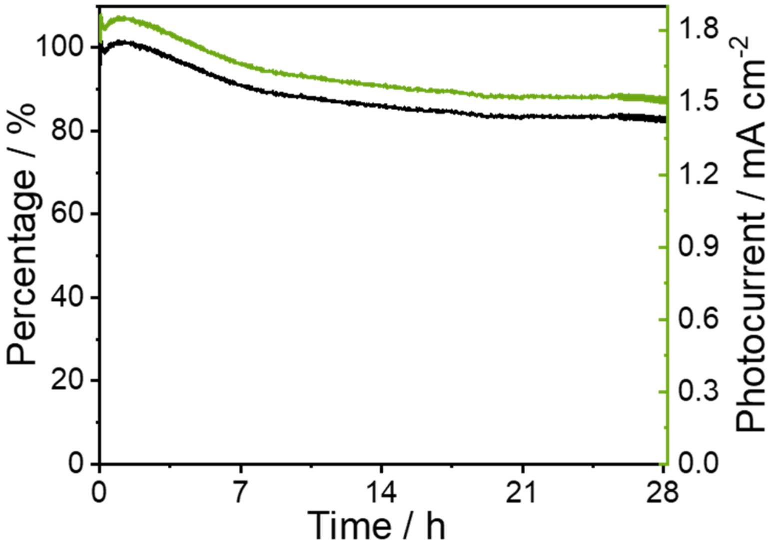

Figure S12. Stability test for 28 h of the Ti–Fe_2O_3/Ni–NC photoanode measured at +1.23 V_{RHE} under 1 sun illumination in 0.5 M glycerol and 1 M NaOH.

Table S1. Thermodynamic free energy corrections applied to DFT-calculated energies at room temperature, taken from ref. [19]. All intermediates were adsorbed on the Cu(211) surface.

Species	Fugacity (Pa)	ZPE (eV)	$\int C_p dT$ (eV)	-TS (eV)
H_2(g)	101325	0.27	0.09	-0.39
H_2O(g)	3534	0.58	0.10	-0.65
CH_3O*	N/A	1.11	0.09	-0.18
CH_2O*	N/A	0.76	0.09	-0.19
CHO*	N/A	0.44	0.09	-0.18
CO*	N/A	0.19	0.08	-0.15
COOH*	N/A	0.62	0.10	-0.18

Table S2. Thermodynamic free-energy corrections applied to DFT-calculated reaction energies for the reduction of CH_3O* to *COOH.

	Reaction	ΔZPE (eV)	$\int \Delta C_P dT$ (eV)	-TΔS (eV)	$\Delta G^{corr} = \Delta ZPE + \int \Delta C_P dT - T\Delta S$ (eV)
#1	$CH_3O^* \rightarrow CH_2O^* + ½H_2(g)$	-0.22	0.04	-0.21	-0.38
#2	$CH_2O^* \rightarrow CHO^* + ½H_2(g)$	-0.18	0.04	-0.19	-0.33
#3	$CHO^* \rightarrow CO^* + ½H_2(g)$	-0.12	0.04	-0.16	-0.25
#4	$CO^* + H_2O \rightarrow COOH^* + ½H_2(g)$	-0.01	-0.04	0.43	+0.38

Based on Table S1-2, the following reaction free-energy corrections were adopted in this work:

$\Delta G_{\mathrm{eq1}}^{\mathrm{corr}} = -0.32$ eV, obtained as the mean value of reactions #1–#3 (standard deviation: 0.05 eV), and $\Delta G_{\mathrm{eq2}}^{\mathrm{corr}} = +0.38$ eV, corresponding to reaction #4.

Table S3. Possible glycerol electro-oxidation reaction intermediates and pathways on Fe–NC.

	Structure	Picture	ΔG/eV	Comments
1st step possibilities, based on $C_3H_8O_3$				
1	CH$_2$OH-CHOH-*CHOH	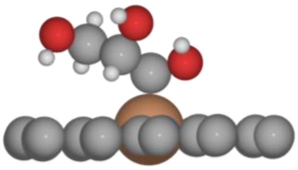	0.66	-1H at 1C
2	CH$_2$OH-CHOH-CH$_2$O*	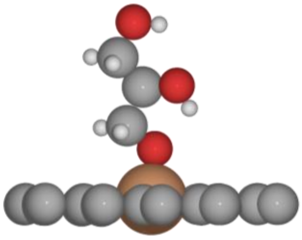	0.34	-1H at 1O
3	CH$_2$OH-*COH-CH$_2$OH	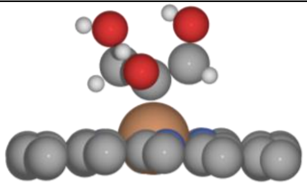	0.77	-1H at 2C
4	CH$_2$OH-CHO*-CH$_2$OH	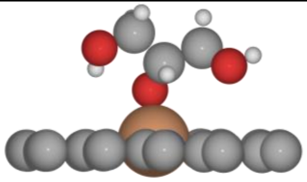	**0.22**	-1H at 2O
5	CH$_2$OH-CH(OH)$_2$+*CH$_2$OH	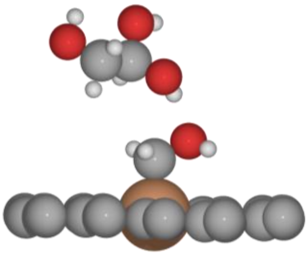	1.38	+1OH at 2C, C1-C2 bond breaks
6	CH$_2$OH-*CHOH+CH$_2$(OH)$_2$	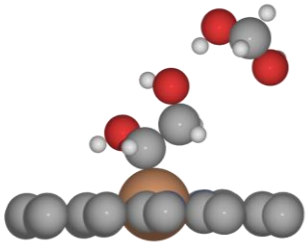	1.15	+1OH at 1C, C1-C2 bond breaks

	Structure	**Picture**	**ΔG/eV**	**Comments**
2nd step possibilities, based on $CH_2OH-CHO^*-CH_2OH$				
1	$CH_2OH-CO-CH_2OH$	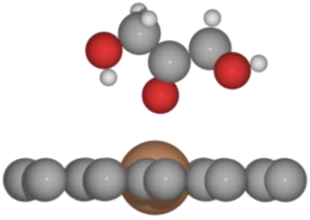	**0.14**	-1H at 2C, C=O double bond formed, molecule desorbs
2	$CH_2OH-CHO+CH_2(OH)_2$	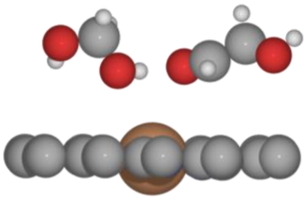	1.12	+1OH at C1, and C1-C2 bond breaks. C2=O2 double bond formed, both molecules desorb
3rd step possibilities, based on $CH_2OH-CO-CH_2OH$				
1	$CH_2OH-CO-^*CHOH$	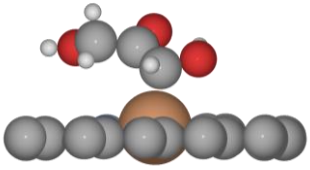	**0.43**	-1H at 1C
2	$CH_2OH-CO-CH_2O^*$	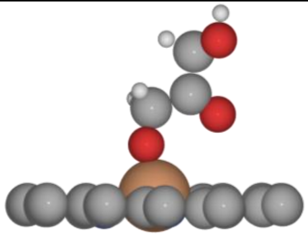	0.55	-1H at 1O
3	$CH_2OH-^*CO+CH_2(OH)_2$	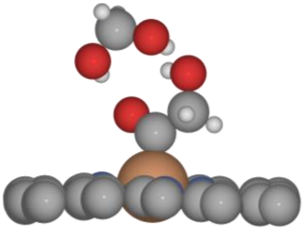	0.70	+1OH at 1 C, C1-C2 bond breaks. One molecule desorbs
4	$CH_2OH-COOH+^*CH_2OH$	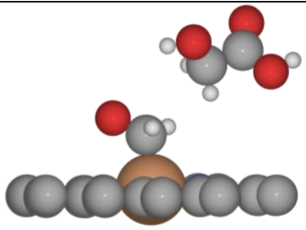	0.88	+1OH at 2 C, C1-C2 bond breaks. One molecule desorbs

	Structure	Picture	ΔG/eV	Comments
5	CH_2OH-C(OH)O*-CH_2OH	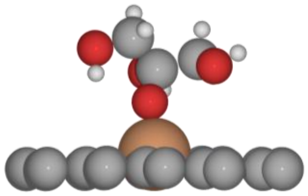	1.04	+1OH at 2C, C2-O2 double bond breaks. Molecule adsorbs via 2O atom
4th step possibilities, based on CH_2OH-CO-*CHOH				
1	CH_2OH-CO-*COH	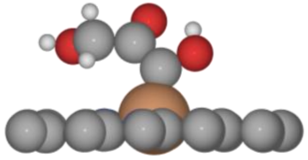	0.96	-1H at 1C
2	CH_2OH-CO-CHO	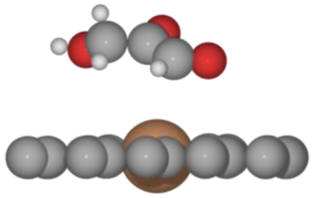	**0.76**	-1H at 1O, C1=O1 double bond forms, desorb
3	CH_2OH-CO-$CH(OH)_2$	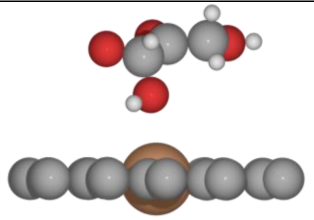	0.95	+1OH at 1C, desorb
4	CH_2OH-COOH+*CHOH	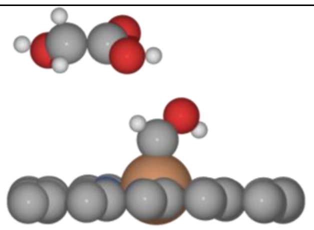	0.84	+1OH at 2C, C1-C2 bond breaks, one molecule desorbs
5th step possibilities, based on CH_2OH-CO-CHO				
1	CH_2OH-CO-*CO	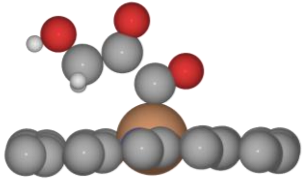	0.74	-1H at 1C
2	CH_2O*-CO-CHO	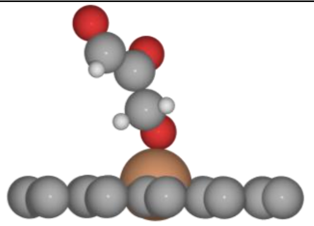	0.78	-1H at 3O

	Structure	**Picture**	**ΔG/eV**	**Comments**
3	*CHOH-CO-CHO	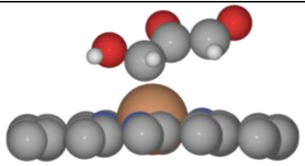	0.89	-1H at 3C
4	CH_2OH-*CO+HCOOH	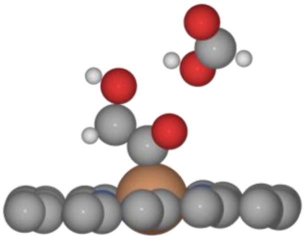	**0.41**	+1OH at 1C, C1-C2 bond break, one molecule desorbs
5	*CH_2OH+COOH-CHO	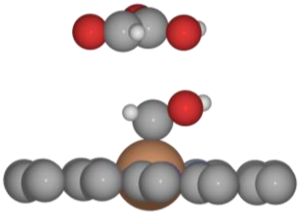	1.33	+1OH at 2C, C2-C3 bond breaks, one molecule desorbs
6	$CH_2(OH)_2$+*CO-CHO	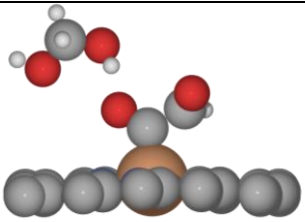	1.15	+1OH at 2C, C2-C3 bond breaks, one molecule desorbs
7	CH_2OH-COOH+*CHO	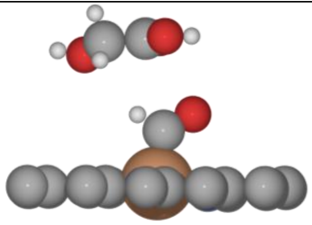	0.55	+1OH at 2C, C2-C1 bond breaks, one molecule desorbs
8	CH_2OH-C(OH)O*-CHO	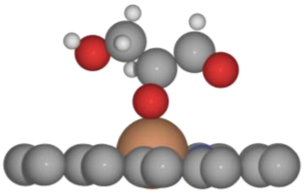	1.25	+1OH at 2C, C2=O2 double bond breaks, adsorb via O2
9	CH_2OH-CO-CH(OH)O*	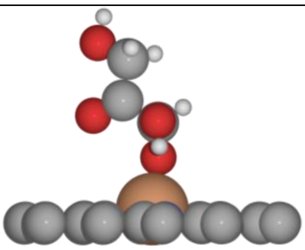	1.32	+1OH at 1O, C1=O1 double bond breaks, adsorb via O1

	Structure	Picture	ΔG/eV	Comments
6th step possibilities, based on CH_2OH-*CO+HCOOH				
1	CH_2OH-COOH+HCOOH	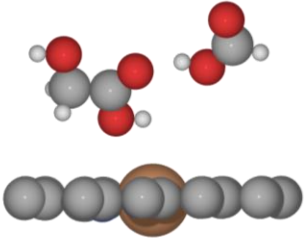	0.51	+1OH at 2C, molecule desorbs
2	$CH_2(OH)_2$+*CO+HCOOH	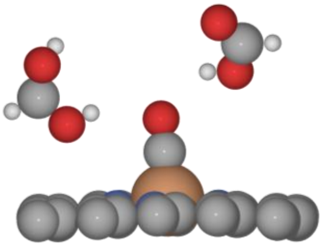	0.21	+1OH at 3C, C3-C2 bond breaks, one molecule desorbs
3	CHOH=CO+HCOOH	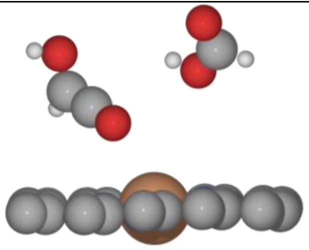	1.54	-1H at 3C, C2=C3 double bond formed, desorb

Table S4. Possible glycerol electro-oxidation reaction intermediates and pathways on Ni–NC.

	Structure	**Picture**	**ΔG/eV**	**Comments**
1st step possibilities, based on $C_3H_8O_3$				
1	CH_2OH-CHOH-*CHOH	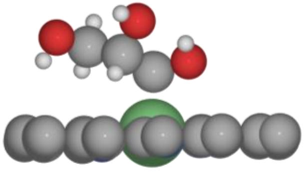	1.75	-1H at 1C
2	CH_2OH-CHOH-CH_2O*	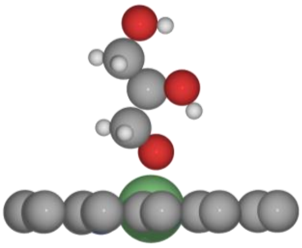	**1.24**	-1H at 1O
3	CH_2OH-*COH-CH_2OH	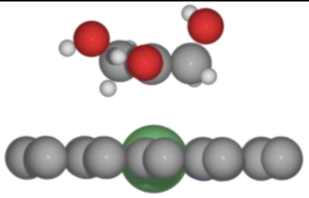	1.65	-1H at 2C
4	CH_2OH-CHO*-CH_2OH	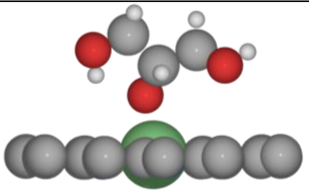	1.40	-1H at 2O
5	CH_2OH- $CH(OH)_2$+*CH_2OH	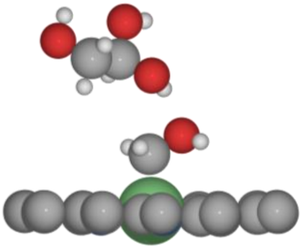	2.37	+1OH at 2C, C1-C2 bond breaks
6	CH_2OH- *CHOH+$CH_2(OH)_2$	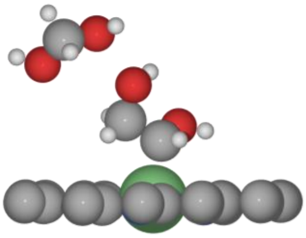	2.65	+1OH at 1C, C1-C2 bond breaks

	Structure	Picture	ΔG/eV	Comments
2^{nd} step possibilities, based on CH_2OH-$CHOH$-CH_2O*				
1	CH_2OH-$CHOH$-CHO	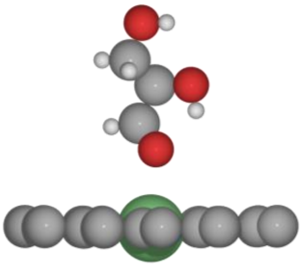	**0.24**	-1H at 1C; C1=O1 double bond formed; desorb
2	CH2OH- $CH(OH)_2$+CH_2O	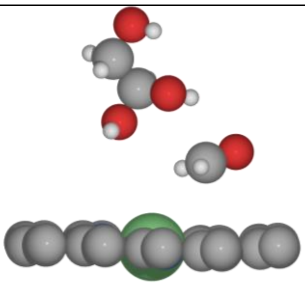	1.39	+1OH at C2; C2-C1 bond breaks; C1=O1 double bond formed; both molecules desorb
3^{rd} step possibilities, based on CH_2OH-$CHOH$-CHO				
1	CH_2OH-$CHOH$-*CO	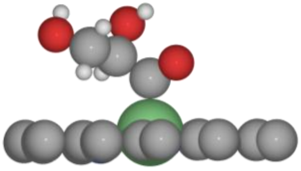	1.16	-1H at 1C
2	CH_2OH-*COH-CHO	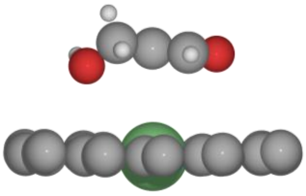	**0.69**	-1H at 2C
3	CH_2OH-CHO*-CHO	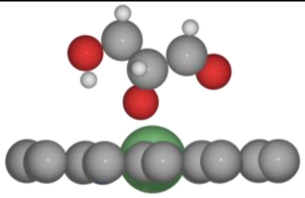	1.47	-1H at 2O
4	*CHOH-CHOH-CHO	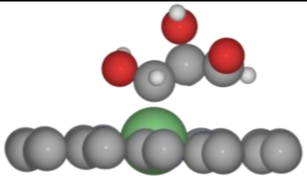	1.95	-1H at 3C
5	CH_2O*-CHOH-CHO	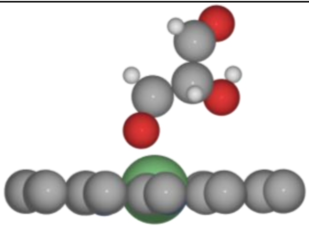	1.57	-1H at 3O

	Structure	**Picture**	**ΔG/eV**	**Comments**
6	$CH_2(OH)_2$+*CHOH-CHO	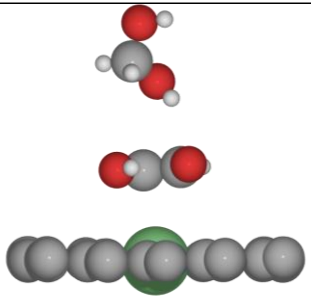	1.70	+1OH at 3C, C3-C2 bond breaks; one molecule desorbs
7	*CH_2OH+$CH(OH)_2$-CHO	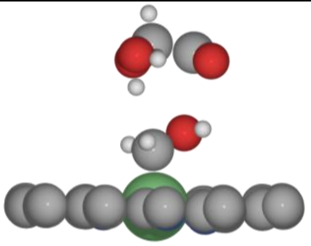	2.65	+1OH at C2, C2-C3 bond breaks; one molecule desorbs
8	CH_2OH-*CHOH+HCOOH	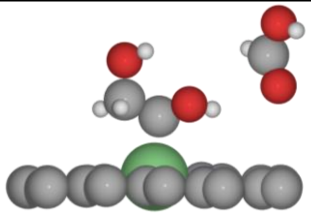	1.72	+1OH at C1, C1-C2 bond breaks; one molecule desorbs.
9	CH_2OH-$CH(OH)_2$+*CHO	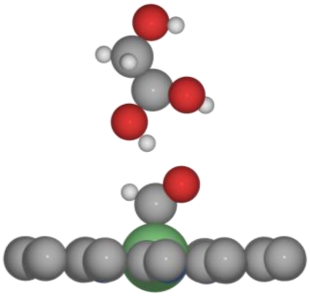	2.15	+1OH at C2, C2-C1 bond breaks; one molecule desorbs
10	CH_2OH-CHOH-CH(OH)O*	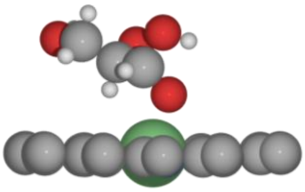	2.14	+1OH at C1, C1=O1 double bond breaks; molecule adsorbs via O atom.
11	CH_2OH-CHOH-*CO	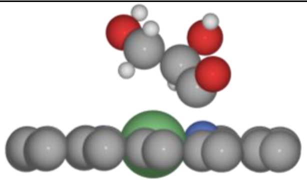	2.09	-1H at 1C, intermediate adsorbs via C atom to N atom

	Structure	**Picture**	**ΔG/eV**	**Comments**
4th step possibilities, based on CH_2OH-*COH-CHO				
1	CH_2OH-$C(OH)_2$-CHO	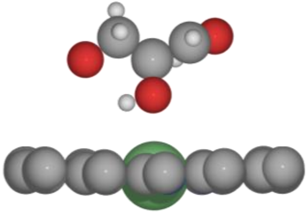	1.08	+1OH at 2C, desorb
2	CH_2OH-CO-CHO	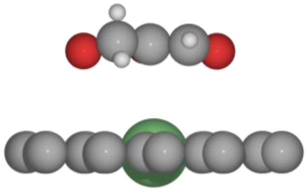	0.45	-1H at 2C, C2=O2 double bond formed; desorb
3	$CH_2(OH)_2$+*COH-CHO	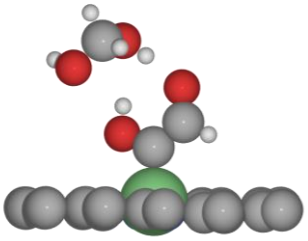	2.87	+1OH at C3, C2-C2 bond breaks; one molecule desorbs
4	CH_2OH-*COH+HCOOH	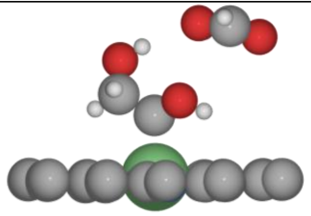	2.99	+1OH at C1, C1-C2 bond breaks; one molecule desorbs
5	CHOH=COH-CHO	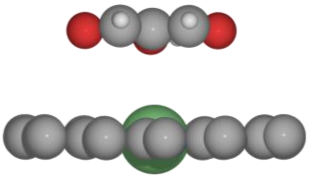	**-0.02**	-1H at C3, C3=C2 double bond formed; desorb
6	CH_2O*-COH-CHO	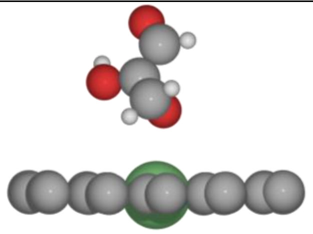	1.00	-1H at O3
7	CH_2OH-COH=CO	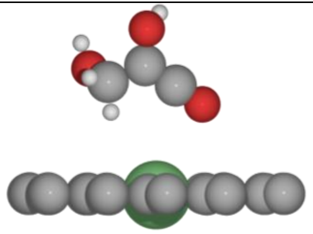	1.16	-1H at C1, C1=C2 double bond formed; desorb

	Structure	**Picture**	**ΔG/eV**	**Comments**
8	$CH_2OH+C(OH)_2-CHO$	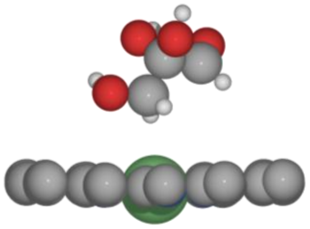	1.16	+1OH at C2, C2-C3 bond breaks; one molecule desorbs. After relaxation, the structure is same with 1.
9	$CH_2OH-C(OH)_2+{}^*CHO$	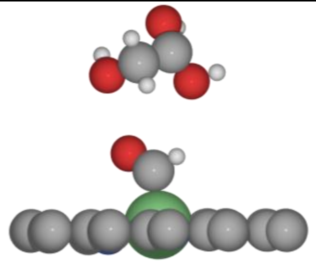	3.68	+1OH at C2, C2-C1 bond breaks; one molecule desorbs
5th step possibilities, based on CHOH=COH-CHO				
1	*COH=COH-CHO	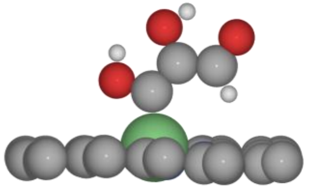	1.73	-1H at C3
2	CHO*=COH-CHO	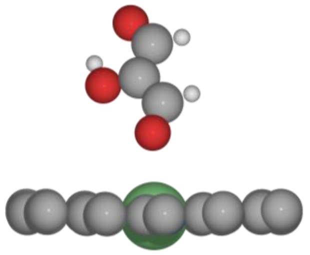	**0.51**	-1H at O3
3	CHOH=CO-CHO	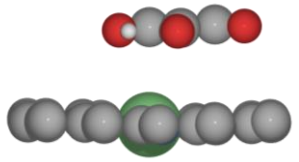	0.80	-1H at O2
4	CHOH=COH-*CO	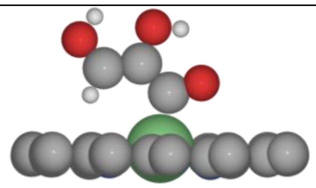	1.35	-1H at C1

	Structure	**Picture**	**ΔG/eV**	**Comments**
5	CHOH=*COH+HCOOH	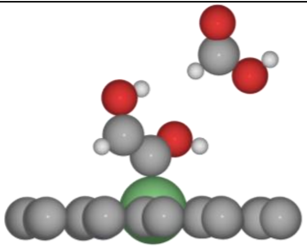	2.46	+1OH at C1, C1-C2 bond breaks; one molecule desorbs
6	CHOH=C(OH)$_2$+*CHO	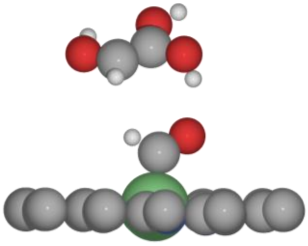	2.69	+1OH at C2, C2-C1 bond breaks; one molecule desorbs
7	CH(OH)$_2$-*COH-CHO	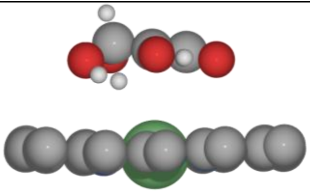	1.74	+1OH at C3, C3=C2 double bond breaks
8	*CHOH-C(OH)$_2$-CHO	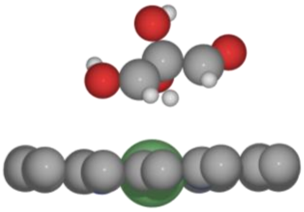	2.86	+1OH at C2, C3=C2 double bond breaks
9	CHOH=COH-CH(OH)O*	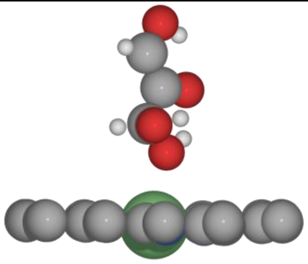	1.60	+1OH at C1, C1=O1 double bond breaks

Table S5. Possible formic acid electro-oxidation reaction intermediates and pathways on Fe–NC.

	Structure	**Picture**	**ΔG/eV**	**Comments**
1st step possibilities, based on HCOOH				
1	*COOH	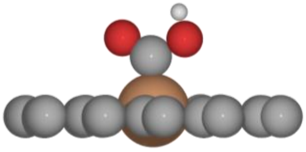	-0.01	-1H at C
2	HCOO*	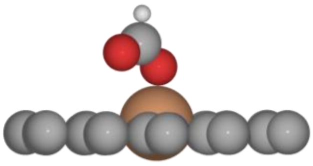	**-0.17**	-1H at O
3	HC(OH)$_2$O*	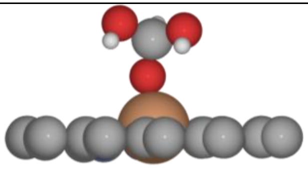	1.34	+1OH at C, C=O double bond breaks, adsorb
2nd step possibilities, based on HCOO*				
1	CO$_2$	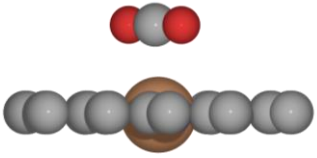	**-0.58**	-1H at C, C=O double bond formed, desorb

Table S6. Possible formic acid electro-oxidation reaction intermediates and pathways on Ni–NC.

	Structure	Picture	ΔG/eV	Comments
1st step possibilities, based on HCOOH				
1	*COOH	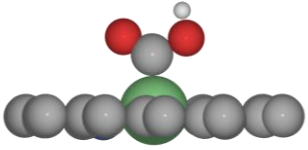	1.13	-1H at C
2	HCOO*	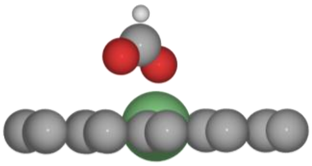	**0.75**	-1H at O
3	$HC(OH)_2O$*	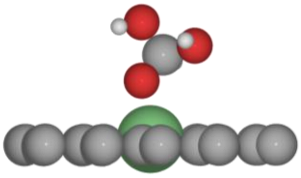	2.21	+1OH at C, C=O double bond breaks, adsorb
2nd step possibilities, based on HCOO*				
1	CO_2	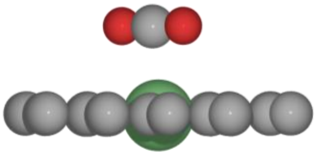	**-0.60**	-1H at C, C=O double bond formed, desorb

References

1. Liu, S.; Mukadam, Z.; Pedersen, A.; Barrio, J.; Parker, J.; Tyrrell, H.; Haigh, S. J.; Titirici, M. M.; Stephens, I. E. L.; Kastlunger, G., Bridging Outer- and Inner-Sphere Electrosynthesis from Biomass-Derived Furfural Using Single Atom Catalysts. *The Journal of Physical Chemistry C* **2025,** *129* (10), 5032-5042.

2. Sarma, S. C.; Barrio, J.; Bagger, A.; Pedersen, A.; Gong, M.; Luo, H.; Wang, M.; Favero, S.; Zhao, C.-X.; Zhang, Q.; Kucernak, A.; Titirici, M.-M.; Stephens, I. E. L., Reaching the Fundamental Limitation in CO2 Reduction to CO with Single Atom Catalysts. *Advanced Functional Materials* **2023,** *33* (41), 2302468.

3. Yang, M.; Oldham, L. I.; Daboczi, M.; Baghdadi, Y.; Cui, J.; Benetti, D.; Zhang, W.; Durrant, J. R.; Hankin, A.; Eslava, S., Advancing Hematite Photoanodes for Photoelectrochemical Water Splitting: The Impact of g-C3N4 Supported Ni-CoP on Photogenerated Hole Dynamics. *Advanced Energy Materials* **2024,** *14* (29), 2401298.

4. Ebeling, K. M.; Bongartz, D.; Mürtz, S.; Palkovits, R.; Mitsos, A., Thermodynamic and Economic Potential of Glycerol Oxidation to Replace Oxygen Evolution in Water Electrolysis. *Industrial & Engineering Chemistry Research* **2024,** *63* (18), 8250-8260.

5. Hjorth Larsen, A.; Jørgen Mortensen, J.; Blomqvist, J.; Castelli, I. E.; Christensen, R.; Dułak, M.; Friis, J.; Groves, M. N.; Hammer, B.; Hargus, C.; Hermes, E. D.; Jennings, P. C.; Bjerre Jensen, P.; Kermode, J.; Kitchin, J. R.; Leonhard Kolsbjerg, E.; Kubal, J.; Kaasbjerg, K.; Lysgaard, S.; Bergmann Maronsson, J.; Maxson, T.; Olsen, T.; Pastewka, L.; Peterson, A.; Rostgaard, C.; Schiøtz, J.; Schütt, O.; Strange, M.; Thygesen, K. S.; Vegge, T.; Vilhelmsen, L.; Walter, M.; Zeng, Z.; Jacobsen, K. W., The atomic simulation environment—a Python library for working with atoms. *J. Phys.: Condens. Matter* **2017,** *29* (27), 273002.

6. Enkovaara, J.; Rostgaard, C.; Mortensen, J. J.; Chen, J.; Dułak, M.; Ferrighi, L.; Gavnholt, J.; Glinsvad, C.; Haikola, V.; Hansen, H. A.; Kristoffersen, H. H.; Kuisma, M.; Larsen, A. H.; Lehtovaara, L.; Ljungberg, M.; Lopez-Acevedo, O.; Moses, P. G.; Ojanen, J.; Olsen, T.; Petzold, V.; Romero, N. A.; Stausholm-Møller, J.; Strange, M.; Tritsaris, G. A.; Vanin, M.; Walter, M.; Hammer, B.; Häkkinen, H.; Madsen, G. K. H.; Nieminen, R. M.; Nørskov, J. K.; Puska, M.; Rantala, T. T.; Schiøtz, J.; Thygesen, K. S.; Jacobsen, K. W., Electronic structure calculations with GPAW: a real-space implementation of the projector augmented-wave method. *J. Phys.: Condens. Matter* **2010,** *22* (25), 253202.

7. Mortensen, J. J.; Hansen, L. B.; Jacobsen, K. W., Real-space grid implementation of the projector augmented wave method. *Phys. Rev. B* **2005,** *71* (3), 035109.

8. Hammer, B.; Hansen, L. B.; Nørskov, J. K., Improved adsorption energetics within density-functional theory using revised Perdew-Burke-Ernzerhof functionals. *Phys. Rev. B* **1999,** *59* (11), 7413-7421.

9. Valter, M.; Santos, E. C. d.; Pettersson, L. G. M.; Hellman, A., Selectivity of the First Two Glycerol Dehydrogenation Steps Determined Using Scaling Relationships. *ACS Catal.* **2021,** *11* (6), 3487-3497.

10. Valter, M.; dos Santos, E. C.; Pettersson, L. G. M.; Hellman, A., Partial Electrooxidation of Glycerol on Close-Packed Transition Metal Surfaces: Insights from First-Principles Calculations. *The Journal of Physical Chemistry C* **2020,** *124* (33), 17907-17915.

11. Liu, B.; Greeley, J., Decomposition Pathways of Glycerol via C–H, O–H, and C–C Bond Scission on Pt(111): A Density Functional Theory Study. *J. Phys. Chem. C* **2011,** *115* (40), 19702-19709.

12. Valter, M.; Busch, M.; Wickman, B.; Grönbeck, H.; Baltrusaitis, J.; Hellman, A., Electrooxidation of Glycerol on Gold in Acidic Medium: A Combined Experimental and DFT Study. *J. Phys. Chem. C* **2018,** *122* (19), 10489-10494.

13. Garcia, A. C.; Kolb, M. J.; van Nierop y Sanchez, C.; Vos, J.; Birdja, Y. Y.; Kwon, Y.; Tremiliosi-Filho, G.; Koper, M. T. M., Strong Impact of Platinum Surface Structure on Primary and Secondary Alcohol Oxidation during Electro-Oxidation of Glycerol. *ACS Catal.* **2016,** *6* (7), 4491-4500.

14. Yan, H.; Yao, S.; Liang, W.; Feng, X.; Jin, X.; Liu, Y.; Chen, X.; Yang, C., Selective oxidation of glycerol to carboxylic acids on Pt(111) in base-free medium: A periodic density functional theory investigation. *Appl. Surf. Sci.* **2019,** *497*, 143661.

15. Wang, Y.; Zhu, Y.-Q.; Xie, Z.; Xu, S.-M.; Xu, M.; Li, Z.; Ma, L.; Ge, R.; Zhou, H.; Li, Z.; Kong, X.; Zheng, L.; Zhou, J.; Duan, H., Efficient Electrocatalytic Oxidation of Glycerol via Promoted OH* Generation over Single-Atom-Bismuth-Doped Spinel Co3O4. *ACS Catal.* **2022,** *12* (19), 12432-12443.

16. Schlegel, N.; Bagger, A.; Rossmeisl, J.; Arenz, M., Elucidating the Reaction Pathway of Glucose Electrooxidation to Its Valuable Products: The Influence of Mass Transport and Electrode Potential on the Product Distribution. *J. Phys. Chem. C* **2023,** *127* (37), 18609-18618.

17. Rossmeisl, J.; Logadottir, A.; Nørskov, J. K., Electrolysis of water on (oxidized) metal surfaces. *Chem. Phys.* **2005,** *319* (1), 178-184.

18. Nørskov, J. K.; Rossmeisl, J.; Logadottir, A.; Lindqvist, L.; Kitchin, J. R.; Bligaard, T.; Jónsson, H., Origin of the Overpotential for Oxygen Reduction at a Fuel-Cell Cathode. *J. Phys. Chem. B* **2004,** *108* (46), 17886-17892.

19. Peterson, A. A.; Abild-Pedersen, F.; Studt, F.; Rossmeisl, J.; Nørskov, J. K., How copper catalyzes the electroreduction of carbon dioxide into hydrocarbon fuels. *Energy Environ. Sci.* **2010,** *3* (9), 1311-1315.

20. Heenen, H. H.; Gauthier, J. A.; Kristoffersen, H. H.; Ludwig, T.; Chan, K., Solvation at metal/water interfaces: An ab initio molecular dynamics benchmark of common computational approaches. *J. Chem. Phys.* **2020,** *152* (14).

21. Barrio, J.; Pedersen, A.; Sarma, S. C.; Bagger, A.; Gong, M.; Favero, S.; Zhao, C.-X.; Garcia-Serres, R.; Li, A. Y.; Zhang, Q.; Jaouen, F.; Maillard, F.; Kucernak, A.; Stephens, I. E. L.; Titirici, M.-M., FeNC Oxygen Reduction Electrocatalyst with High Utilization Penta-Coordinated Sites. *Advanced Materials* **2023,** *35* (14), 2211022.